

Solidification of Hastelloy Alloys: an Alternative Interpretation

M.J. PERRICONE, J.N. DUPONT, and M.J. CIESLAK

HASTELLOY C-22 and C-276 are engineering nickel-based alloys that served as the focus of a comprehensive examination of the microstructural development of this class of materials presented previously by Cieslak *et al.* The work presented here provides a re-examination of this study. The use of computational thermodynamic algorithms combined with solidification-path calculations based on experimentally determined solute-partition data eliminates the need for many assumptions and serves as the basis for the solute-redistribution model that is presented here. A new series of solidification sequences for HASTELLOY C-22 and C-276 is proposed based on this model, and these conclusions are supported by the microstructural characterization presented in the previous work.

I. INTRODUCTION

HASTELLOY* alloys are nickel-based materials that

*HASTELLOY is a trademark of Haynes International, Kokomo, IN.

are often used in corrosive environments, as well as for filler metal in stainless steel welds.^[3,4,5] The study of the HASTELLOY C-22 and C-276 alloys presented by Cieslak *et al.*^[1] provided a detailed description of the microstructural development in fusion welds of these alloys and serves as the focus of the work presented here. Based on detailed microstructural analysis, a set of phase-transformation sequences under normal arc-welding conditions was proposed. An understanding of the solidification sequence was somewhat limited by the lack of a Ni-Cr-Mo liquidus projection at the time of publication, requiring a number of assumptions to be made in the interpretation of the experimental results. Recent advances have led to the development of thermodynamic algorithms that enable the development of *multicomponent* phase diagrams that more accurately describe the behavior of these engineering alloys. Consequently, many of the simplifying assumptions used previously^[1] can be eliminated, and calculated phase diagrams can be combined with solidification theory to more accurately explain microstructural development in these alloys. This article applies the combination of calculated multicomponent liquidus projections and solute-redistribution simulations toward an improved interpretation of the microstructural development of fusion welds in HASTELLOY alloys.

II. MODELING MICROSTRUCTURAL DEVELOPMENT DURING SOLIDIFICATION

The CALPHAD program used for this research is Thermo-Calc Version N^[6,7] combined with the Nickel Alloy Database developed by THERMOTEC* Ltd.^[8] This software

*THERMOTEC is a trademark of Thermotech Ltd., UK.

M.J. PERRICONE, Graduate Research Assistant, and J.N. DuPONT, Associate Professor, are with the Department of Materials Science and Engineering, Lehigh University, Bethlehem, PA 18015. Contact e-mail: mjp2@lehigh.edu M.J. CIESLAK, Director, Materials and Processes Center, is with the Materials and Process Sciences Center, Sandia National Laboratory, Albuquerque, NM 87185.

Manuscript submitted March 27, 2002.

determines phase stability through a free-energy-minimization calculation based on published thermodynamic data that has been assessed and assembled into a database. Initial work with this computational thermodynamic technique involved the calculation of a ternary liquidus surface for the Ni-Cr-Mo system to serve as a basis for the database validation. The molar fraction of the liquid phase was maintained at 1, while the temperature and the composition of the system were varied using a map function until all lines of twofold saturation were delineated, terminating either at a compositional axis or a ternary eutectic point. The invariant points on the resulting liquidus projection (Figure 1(a)) were then compared to those on an estimated Ni-Cr-Mo liquidus projection based on experimental results^[9] (Figure 1(b)), and reasonable agreement between the data is shown in Table I.

Once these preliminary calculations were completed, efforts focused on the improvement of the previous study^[1] on the Ni-based HASTELLOY C-22 and C-276 alloys, the compositions of which are displayed in Table II. Solidification-path calculations for each alloy were completed using the Mehrabian-Flemings model,^[10] the equation for which is

$$C_{l,Mo} = C_{0,Mo} \left(\frac{C_{l,Cr}}{C_{0,Cr}} \right)^{\frac{k_{Mo}-1}{k_{Cr}-1}} \quad [1]$$

where:

- $C_{l,i}$ = composition in liquid of element i ,
- $C_{0,i}$ = nominal composition of element i , and
- k_i = partition coefficient for element i

This solidification model operates on the same assumptions as the Scheil equation for non-equilibrium solidification: dendrite-tip undercooling and solid-state diffusion of each solute are negligible, thermodynamic equilibrium is maintained at the solid/liquid interface, and diffusion is infinitely fast in the liquid. The implications for the solidification model when these restrictions are relaxed will be discussed in detail in the proceeding sections. The model tracks the Mo content of the liquid as a function of the nominal Mo and nominal Cr compositions, as well as the Cr content of the liquid during solidification. Although other alloying elements are present in small amounts, it is assumed that their effect on solidification behavior can be accounted for by the position of the lines of twofold saturation in the multicomponent liquidus projection presented subsequently and,

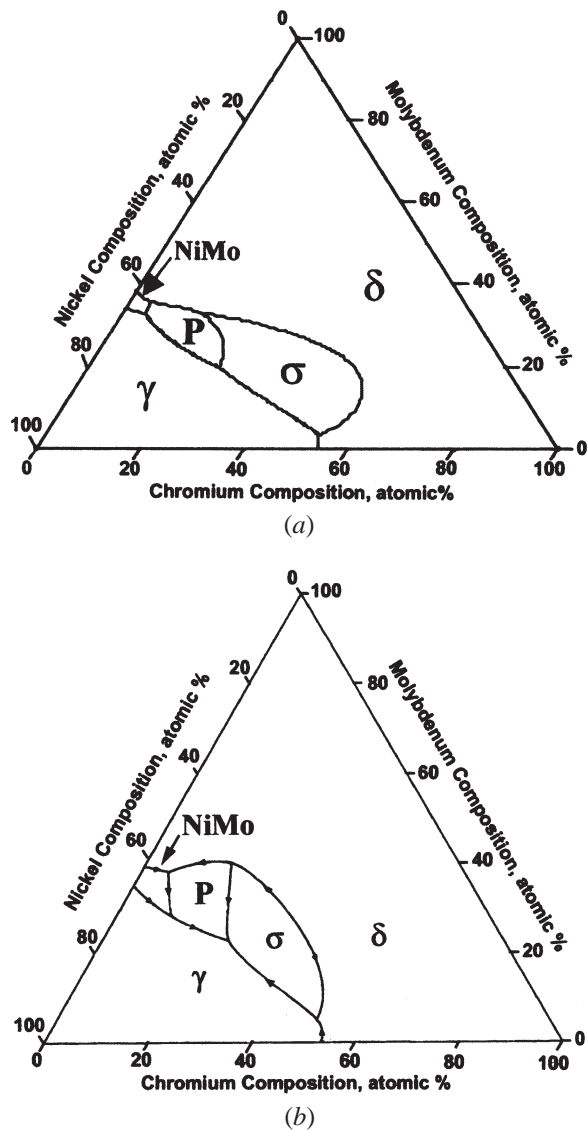


Fig. 1—(a) Calculated Ni-Cr-Mo ternary liquidus projection, where compositions are expressed in atomic fraction. (b) Approximate liquidus projection for Ni-Cr-Mo proposed by Gupta,^[9] where compositions are expressed in atomic percent.

therefore, need not be included directly in the solidification-path calculation (*i.e.*, the effect of these higher-order elements on solidification is to change the position of the twofold saturation lines). The direction of the solidification path is determined by k_{Mo} and k_{Cr} , which are partition coefficients that govern solute redistribution during solidification and have been experimentally measured in previous work.^[2] The primary solidification paths were calculated using Eq. [1], using these experimentally measured partition-coefficient values as constants. The result of the combination of the liquidus projection with the solidification-path calculation provides a prediction of the solidification sequence of each alloy. These data were then compared to the solidification sequences proposed by Cieslak *et al.*,^[1] as discussed in the next section.

Table I. Invariant Point Comparison for Figure 1

Invariant Point	This Work (Figure 1(a)), At. Pct	Gupta ^[9] (Figure 1(b)), At. Pct
NiMo- δ	38Mo	39Mo
NiMo- δ -P	36Mo, 4Cr	38Mo, 5Cr
NiMo- γ	34Mo	35Mo
NiMo- γ -P	33Mo, 4Cr	28Mo, 12Cr
P- δ - σ	33Mo, 15Cr	40Mo, 17Cr
P- γ - σ	20Mo, 25Cr	23Mo, 24Cr
γ - σ - δ	3Mo, 53Cr	5Mo, 50Cr
γ - δ	54Cr	54Cr

Table II. Alloy Compositions (All Values Are in Wt Percent)

Element	HASTELLOY C-22	HASTELLOY C-276
C	0.006	0.003
Co	0.84	0.96
Cr	21.22	15.83
Fe	3.17	5.44
Mn	0.31	0.50
Mo	13.43	15.56
Ni	56.96	55.58
P	0.010	0.014
S	<0.002	0.002
Si	<0.02	0.03
Ti	0.03	<0.01
V	0.14	0.18
W	3.29	3.93

III. RESULTS/DISCUSSION

The previous study^[1] focused on the welding metallurgy of HASTELLOY C-22 and C-276, both of which are Ni-based alloys with significant Mo alloy additions. HASTELLOY C-4 was also studied previously, but has intentional Ti alloying additions in its composition. The use of Ti as an alloying addition, even in small amounts, can significantly affect the solidification behavior of the material. For this reason, alloy C-4 is not examined in the analysis presented here. In the previous study,^[1] gas-tungsten arc (GTA) welds were prepared autogeneously on each of the materials, and a thorough microstructural analysis was conducted. These experimental data, integrated with “equivalent” compositions developed from isothermal sections of the Ni-Cr-Mo ternary system, were then used to propose a series of phase-transformation sequences. To accomplish this task, these modified equivalent compositions (listed in Table III) served as the starting point of paths tracking solid compositions from the dendrite core to the interdendritic region plotted on these isothermal sections of the Ni-Cr-Mo ternary-phase diagram at 1250 °C and 850 °C, as shown in Figures 2(a) and (b)), respectively. In this figure, the start of the tail of each arrow indicates the dendrite-core composition of each alloy, the length of the arrow tracks the transition in solid composition, and the head of the arrow indicates the interdendritic composition. Note that these isothermal sections track the *solid* alloy composi-

Table III. Alloy Compositions (Weight Percent) Used for Solidification Simulations Displayed in Figure 3

Alloy	Figure	Ni	Cr	Mo	Fe	W
C-22 (previous work)	3A	62.06	21.22	16.72	—	—
C-22 with Fe included	3B	58.89	21.22	16.72	3.17	+
C-22 with Fe and W included	3C	58.89	21.22	13.43	3.17	3.29
C-276 (previous work)	3A	64.68	15.83	19.49	—	—
C-276 with Fe included	3D	59.24	15.83	19.49	5.44	+
C-276 with Fe and W included	3E	59.24	15.83	15.56	5.44	3.93

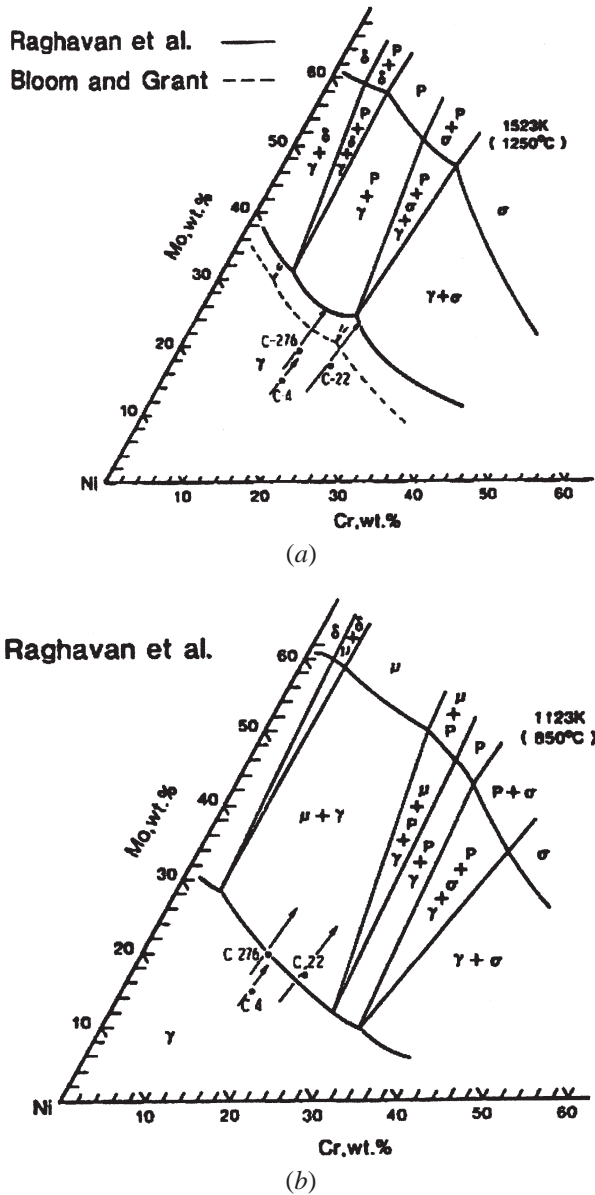


Fig. 2—Isothermal sections^[13,14] of the Ni-Cr-Mo system at (a) 1250 °C and (b) 850 °C showing the equivalent compositions of the alloys examined in the study by Cieslak *et al.*^[1] The alloy C-4 was also a subject of the previous study, but was not involved in the models presented here due to the presence of intentional Ti alloying additions in its composition.

tions rather than the *liquid* composition; thus, they do not provide direct determination of the solidification sequence. More importantly, C-22 and C-276 are not true ternary alloys (compositions are shown in Table II) and, therefore, the use

of pure ternary diagrams to model their behavior introduces error into the analysis. In the previous work, equivalent compositions, displayed in Table III, were used in order to compensate for small amounts of other alloying elements. However, this approach cannot account for the influence of quaternary and higher-order alloy additions on the position of the lines of twofold saturation and the resultant solidification sequence.

In order to improve this model, all of the major alloying elements present within the material must be included in the solidification simulation. The development of the liquidus projections presented in Figure 3 is the result of a series of calculations conducted using the computational thermodynamic algorithms discussed in previous sections. The progressive addition of alloying elements into these thermodynamic calculations is illustrated in Figure 3. The liquidus projection 3A contains only Ni-Cr-Mo, onto which the equivalent nominal compositions and calculated solidification paths for C-22 and C-276 are plotted. The result of the inclusion of Fe into the solidification simulation is displayed in the liquidus projections for C-22 and C-276, shown in Figures 3(b) and (d), respectively. The liquidus projections in Figure 3(c) (C-22) and 3(c) (C-276) include *both* Fe and W in the simulation and, therefore, represent the most comprehensive multicomponent solidification model for this material system. The solid lines in these liquidus projections indicate the positions of lines of twofold solid saturation. Arrowheads have been placed on each of these lines to indicate the direction of decreasing temperature. The nominal composition of the material in each diagram (listed in Table III) is marked with a large black dot. The arrow extending from this point is a graphical representation of the solidification path of the material, as calculated using the Mehrabian–Flemings model^[10] and based on experimentally determined solute-partition data.^[2] The solidification sequence can then be determined through the combination of the calculated liquidus projection and the primary solidification-path calculation. For example, in Figure 3(b), the nominal composition of C-22 falls in the primary γ -phase field, and the solidification path tracks the liquid composition to the line of twofold solid saturation between the γ and σ phase, as indicated by the arrow. At this point, the fraction of liquid is still greater than zero, and the liquid composition will continue to change along the γ/σ line of twofold saturation. As dictated by the directionality of this line with decreasing temperature, the liquid composition will continue to change until either the fraction of liquid reaches zero or the liquid composition reaches the γ - σ -P ternary eutectic point, at which point solidification must terminate. Assuming that no backdiffusion occurs in the solid, the resulting predicted solidification sequence in Figure 3(b) is, therefore,

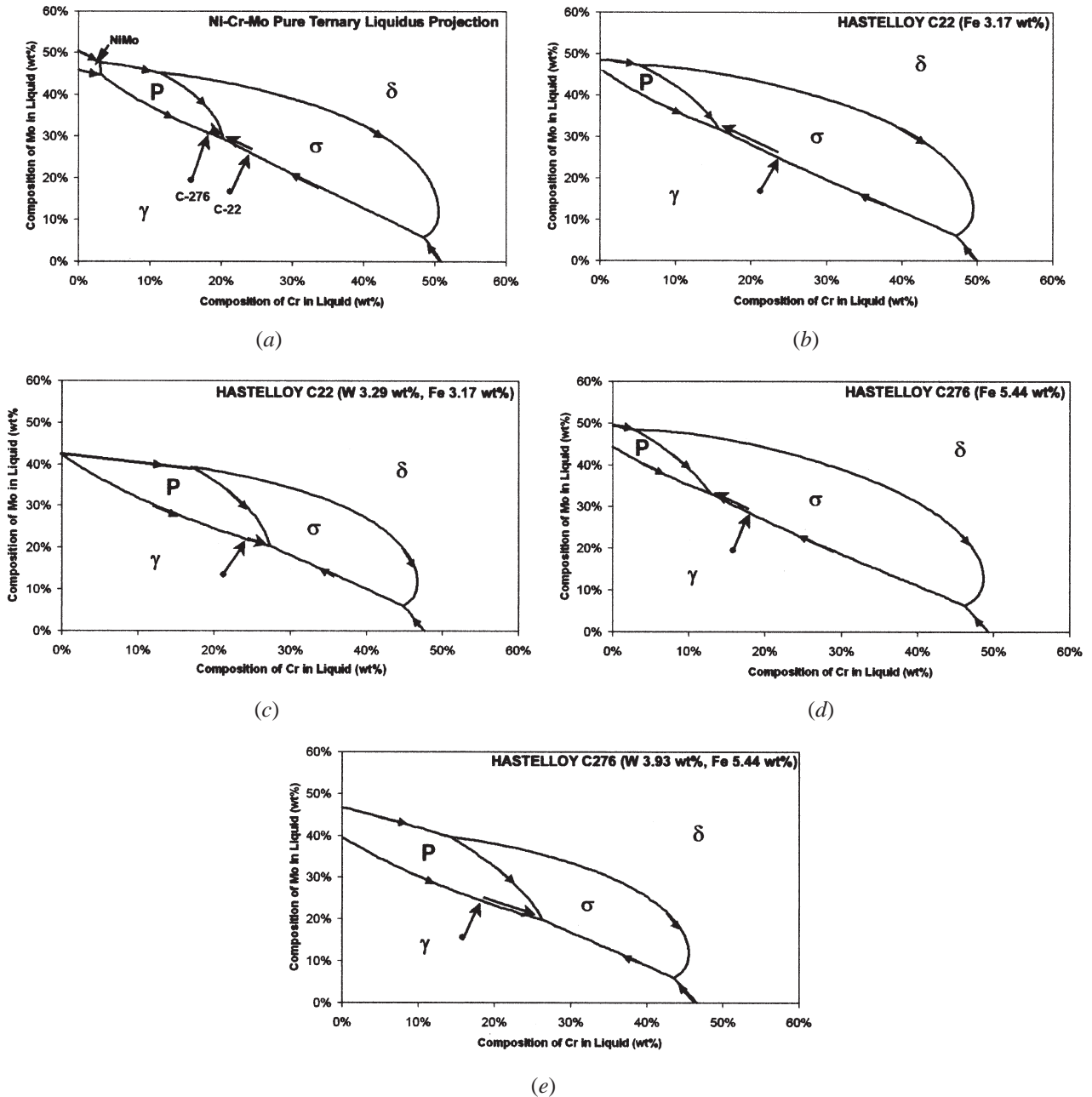


Fig. 3—Calculated Ni-Cr-Mo pseudo-ternary liquidus surfaces where (a) Mo and Ni equivalent compositions (shown in Table II) are plotted on pure Ni-Cr-Mo space, (b) Fe is included for HASTELLOY C-22, (c) Fe and W are included for C-22, (d) Fe is included for HASTELLOY C-276, and (e) Fe and W are included for C-276. Note the stabilization of the P phase due to W. The arrows in each diagram are the calculated solidification paths as determined by the Mehrabian–Flemings^[10] model, and the tail of the first arrow for each alloy is positioned exactly at the nominal composition.

$L \rightarrow L + \gamma \rightarrow L + \gamma + \sigma \rightarrow L + \gamma + \sigma + P \rightarrow \gamma + \sigma + P$. A comparison of the solidification sequences predicted here and the overall transformation sequence presented previously^[1] for C-22 and C-276 are shown in Table IV and V, respectively.

Comparison of the sequences predicted by the multi-component solidification simulations in Figures 3(c) and 3(e) and those proposed previously for each material reveals obvious differences. The simulation pertaining to HASTELLOY C-276 (Figure 3(e)), which predicted the formation of the P and σ phase during solidification, did not coincide with the conclusions of the previous study,

which found no evidence of the presence of σ phase in the microstructure. This contradiction between simulation and experiment can be explained when one considers the mechanisms of microstructural development during solidification. One of the major assumptions of this solute-redistribution model is the absence of backdiffusion of solute in the solid during solidification. For the solidification rates present during the GTA welding process on which the previous study was based, this assumption may not completely describe the behavior of the system, meaning that less solute-rich liquid was present at the termination of solidification. Furthermore, although it was originally assumed that dendrite-

Table IV. Solidification Sequence Comparison for HASTELLOY C-22

Source	Elements	Solidification Sequence
Figure 3(a)	Ni-Cr-Mo	$L \rightarrow L + \gamma \rightarrow L + \gamma + \sigma \rightarrow L + \gamma + \sigma + P \rightarrow \gamma + \sigma + P$
Figure 3(b)	Ni-Cr-Mo-Fe	$L \rightarrow L + \gamma \rightarrow L + \gamma + \sigma \rightarrow L + \gamma + \sigma + P \rightarrow \gamma + \sigma + P$
Figure 3(c)	Ni-Cr-Mo-Fe-W	$L \rightarrow L + \gamma \rightarrow L + \gamma + P \rightarrow L + \gamma + P + \sigma \rightarrow \gamma + P + \sigma$
Previous study	Ni-Cr-Mo	$L \rightarrow L + \gamma \rightarrow L + \gamma + \sigma \rightarrow \gamma + \sigma \rightarrow \gamma + \sigma + P$

Table V. Solidification Sequence Comparison for HASTELLOY C-276

Source	Elements	Solidification Sequence
Figure 3(a)	Ni-Cr-Mo	$L \rightarrow L + \gamma \rightarrow L + \gamma + P \rightarrow L + \gamma + P + \sigma \rightarrow \gamma + P + \sigma$
Figure 3(d)	Ni-Cr-Mo-Fe	$L \rightarrow L + \gamma \rightarrow L + \gamma + \sigma \rightarrow L + \gamma + \sigma + P \rightarrow \gamma + \sigma + P$
Figure 3(e)	Ni-Cr-Mo-Fe-W	$L \rightarrow L + \gamma \rightarrow L + \gamma + P \rightarrow L + \gamma + P + \sigma \rightarrow \gamma + P + \sigma$
Previous study	Ni-Cr-Mo	$L \rightarrow L + \gamma \rightarrow L + \gamma + P \rightarrow \gamma + P$

tip undercooling effects were negligible, the dendrite-tip undercooling during GTA welding by the solute rejection ahead of the solidification front can be significant.^[11] When these two restrictions are relaxed, the liquid may no longer continue to be enriched in solute until the ternary eutectic forms at the termination of solidification. Rather, abbreviated versions of the solidification sequences presented in Tables IV and V may be necessary in order to accurately describe the behavior of HASTELLOY C-22 and C-276, as explained subsequently.

These phenomena, combined with a quantitative determination of the fraction of liquid available to form eutectic in Figures 3(c) and (e), can be used to explain the development of the microstructures characterized previously.^[11] The fraction of total eutectic can be calculated using a modification^[12] of the same Mehrabian–Flemings^[10] model used to calculate the solidification paths presented in this discussion:

$$f_e = \left(\frac{C_{e,Mo}}{C_{0,Mo}} \right)^{\frac{1}{k_{Mo}-1}} \quad [2]$$

where:

- f_e = fraction of eutectic,
- $C_{e,Mo}$ = eutectic composition of Mo,
- $C_{0,Mo}$ = nominal composition of Mo, and
- k_{Mo} = partition coefficient for Mo

The fraction of total eutectic is identical to the fraction of liquid present when the solidification path intersects the line of twofold saturation on the multicomponent liquidus projection. The composition marked by this intersection is regarded as the eutectic composition. The results of these calculations are displayed in Table VI.

The fraction of liquid calculated here represents the maximum amount of liquid that can be present to form eutectic. However, if the restriction that neither backdiffusion nor dendrite-tip undercooling is present is relaxed, the amount of liquid present at the termination of solidification will be reduced. The implications of this reduction for the final solidification sequences can explain the differences between the sequences presented here and those presented previously.^[11] Despite the presence of 6 pct liquid at the ter-

Table VI. Fraction Eutectic Results for HASTELLOY C-22 and C-276

Alloy	C_0 (Wt Pct)	C_e (Wt Pct)	k_{Mo}	Fraction Eutectic
C-22	13.43	22.10	0.82	0.06
C-276	15.56	24.84	0.805	0.09

mination of primary solidification in C-22, the close proximity of the intersection point of the solidification path and the line of twofold saturation between the γ and P phases to the ternary eutectic point for HASTELLOY C-22 (Figure 3(c)) strongly suggests that the ternary eutectic was reached for this alloy; thus, the presence of the σ phase in the microstructure.

However, the comparatively large variation in the liquid composition required to reach the ternary eutectic from the intersection of the primary solidification path and the line of twofold saturation between the γ and P phases in HASTELLOY C-276 (Figure 3(c)) makes the formation of ternary eutectic improbable, considering that a maximum of only 9 pct liquid is present at this intersection. Consequently, the σ phase will not form, resulting in a microstructure that contains P phase in a γ matrix, which is consistent with the microstructural characterization presented previously. Hence, an adjustment must be made to the predicted solidification sequence for this alloy (presented in Table V) to reflect the lack of σ phase in the observed microstructure. Note that the resulting sequence ($L \rightarrow L + \gamma \rightarrow L + \gamma + P \rightarrow \gamma + P$) is the same as that proposed for C-276 in the previous work.^[11]

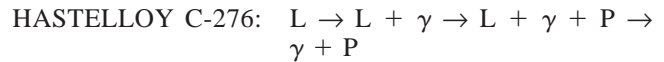
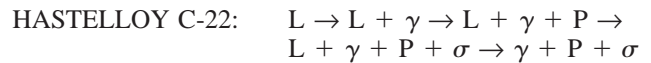
While no modification of the predicted sequence is required to describe the microstructural evolution of HASTELLOY C-22 for the reasons discussed previously, further inspection of the solidification sequences for HASTELLOY C-22 reveals that the major difference between the sequence presented here and that proposed previously involves the formation of the P phase, whether it is a *solidification* product (as predicted in this work) or the result of a solid-state transformation (as previously proposed). Both conclusions are supported by the microstructural analysis presented previously. The presence of P phase in the resultant microstructure of C-22 GTA welds, combined with *isothermal* thermodynamic data, previously seemed to suggest that the P phase was a product of a solid-state transformation.

However, the reason for differing results can be seen by re-examining one of the main assumptions made previously, namely, that W behaves identically to Mo during solidification and, therefore, can be included with Mo in an equivalent Mo composition. The implications of this assumption can be seen in the series of solidification simulations illustrated in Figure 3, which show very different behavior for C-22 and C-276 when they are described in the Ni-Cr-Mo-Fe system (with the W content included in the total Mo content) than when they are described in the Ni-Cr-Mo-Fe-W system (with W considered individually). This difference can be attributed to the expansion of the primary P-phase field when W is included in the liquidus-projection calculation, indicating that the presence of W stabilizes the P phase as a secondary solidification product. This is consistent with the high W content of the P phase determined previously,^[1] as the P phase contains more W than the γ or σ phases.

The results presented here also illustrate the importance of including the effect of all alloying elements in the simulations. For example, note that the sequences predicted when only Fe was included in the calculations for Figures 3(b) and (d) differ a great deal from those predicted by the simulations involving both Fe and W, shown in Figures 3(c) and (e). In fact, the result obtained for the addition of *Fe only* (in Figure 3(d)) does not agree with the microstructural evidence.^[1] Consequently, it is essential to include as many alloying elements as possible in developing solidification models, to ensure an accurate prediction of microstructural development. It is important to note that the consistency between the two sequences for C-276, as shown in Figure 3(a) (Ni-Cr-Mo) and Figure 3(e) (Ni-Cr-Mo-Fe-W), can be explained by the fact that the nominal Mo composition was so high in this alloy that the solidification path intersects the γ /P line of twofold solid saturation before the γ/σ line, with or without the stabilization of the P phase provided by the presence of W.

IV. CONCLUSIONS

Solidification simulations were conducted for the HASTELLOY C-22 and C-276 alloys by combining *multi component* liquidus projections with solidification-path calculations. The analysis of the comprehensive solidification simulations, involving all five of the main elemental constituents (Ni, Cr, Mo, Fe, and W) for HASTELLOY C-22 and C-276, resulted in the proposal of new solidification sequences for these nickel-based alloys.



These sequences represent a small departure from those proposed in the previous study.^[1] However, microstructural and experimental data presented in that publication are consistent with the conclusions reached here.

ACKNOWLEDGMENTS

This work was supported by the Office of Naval Research, under Contract No. N00014-00-1-0448. The authors also acknowledge the American Welding Society's support of this work through a Graduate Research Fellowship. M.J. Cieslak was supported by Sandia Corporation, a Lockheed Martin Company, through the United States Department of Energy's National Nuclear Security Administration under Contract No. DE-AC04-94AL58000.

REFERENCES

1. M.J. Cieslak, T.J. Headley, and A.D. Romig, Jr.: *Metall. Trans. A*, 1986, vol. 17A, pp. 2035-47.
2. S.W. Banovic, J.N. DuPont, and A.R. Marder: *Sci. Technol. Welding Joining*, 2002, vol. 7(5).
3. M.J. Cieslak: *Welding J.*, 1991, vol. 70, pp. 49s-56s.
4. J.N. DuPont: *Metall. Trans. A*, 1996, vol. 27A, pp. 3612-20.
5. J.A. Brooks and A.D. Gardea: *Microstr. Sci.*, 1993, vol. 20, pp. 3-15.
6. B. Sundmann, B. Jansson, and J.O. Andersson: *CALPHAD*, 1985, vol. 9, p. 153.
7. B. Sundman: *Thermo-Calc. [Version N]. 2001*, KTH, Stockholm, 1996.
8. N. Saunders: *Ni-Data Thermodynamic Database. [Version 4.0]*. Thermotech, Ltd., The Surrey Research Park, Guildford, United Kingdom, 2000.
9. K.P. Gupta: *Phase Diagrams of Ternary Nickel Alloys. Part I*, Indian Institute of Metals, Calcutta, 1990.
10. R. Mehrabian and M.C. Flemings: *Metall. Trans.*, 1970, vol. 1, pp. 455-64.
11. J.A. Brooks, M.I. Baskes, and F.A. Greulich: *Metall. Trans. A*, 1991, vol. 22A, pp. 915-26.
12. J.N. DuPont, C.V. Robino, and A.R. Marder: *Acta Mater.*, 1998, vol. 46, pp. 4781-90.
13. D.S. Bloom and N.J. Grant: *Trans. TMS-AIME*, 1954, pp. 261-68.
14. M. Raghavan, R.R. Mueller, G.A. Vaughn, and S. Floreen: *Metall. Trans. A*, 1984, vol. 15A, pp. 783-92.